Commun. Comput. Phys.
doi: 10.4208/cicp.160115.150915a

Vol. **18**, No. 5, pp. 1264-1281
November 2015

High Order Numerical Simulation of Detonation Wave Propagation Through Complex Obstacles with the Inverse Lax-Wendroff Treatment

Cheng Wang[1,*], Jianxu Ding[1], Sirui Tan[2] and Wenhu Han[3]

[1] *State Key Laboratory of Explosion Science and Technology, Beijing Institute of Technology, Beijing, 100081, P.R. China.*
[2] *Division of Applied Mathematics, Brown University, Providence, RI 02912, USA.*
[3] *Center for Combustion Energy, Tsinghua University, Beijing, 100084, P.R. China.*

Communicated by Chi-Wang Shu

Received 16 January 2015; Accepted (in revised version) 15 September 2015

Abstract. The high order inverse Lax-Wendroff (ILW) procedure is extended to boundary treatment involving complex geometries on a Cartesian mesh. Our method ensures that the numerical resolution at the vicinity of the boundary and the inner domain keeps the fifth order accuracy for the system of the reactive Euler equations with the two-step reaction model. Shock wave propagation in a tube with an array of rectangular grooves is first numerically simulated by combining a fifth order weighted essentially non-oscillatory (WENO) scheme and the ILW boundary treatment. Compared with the experimental results, the ILW treatment accurately captures the evolution of shock wave during the interactions of the shock waves with the complex obstacles. Excellent agreement between our numerical results and the experimental ones further demonstrates the reliability and accuracy of the ILW treatment. Compared with the immersed boundary method (IBM), it is clear that the influence on pressure peaks in the reflected zone is obviously bigger than that in the diffracted zone. Furthermore, we also simulate the propagation process of detonation wave in a tube with three different widths of wall-mounted rectangular obstacles located on the lower wall. It is shown that the shock pressure along a horizontal line near the rectangular obstacles gradually decreases, and the detonation cellular size become large and irregular with the decrease of the obstacle width.

AMS subject classifications: 65M06, 76L05

Key words: Boundary treatment, detonation, inverse Lax-Wendroff, two-step reaction model, WENO scheme.

*Corresponding author. *Email address:* wangcheng@bit.edu.cn (C. Wang)

1 Introduction

Studies of the propagating detonation wave in a tube with complex boundaries are an important research field for not only fundamental sciences, but also engineering applications, which usually requires numerical simulations be carried out for the intricate geometries intersecting the Cartesian meshes in an arbitrary fashion. Even though a high order numerical scheme in the internal computational domain is adopted, most of boundary treatments based on the Cartesian grids are not more than the second order accuracy in the vicinity of the complex boundaries. The numerical error caused by a traditional and low order boundary treatment may pollute the results of the internal computational domain. Recently, some successful boundary treatment techniques based on the Cartesian grids are proposed and developed. The reflection technique [1] is a very simple and popular boundary treatment method, in which all physical variables are reflected symmetrically on the rigid wall except for the anti-symmetric normal velocity. This method works well when the rigid boundary is straight and positioned at half points. However, large errors might be caused when such method is applied to complex boundary [2]. Later, the IBM first proposed by Peskin [3] has been numerously modified and refined to deal with both incompressible flows and compressible flows including strong shock waves. Sjögreen et al. [4] developed an embedded boundary finite difference technique with the second order accuracy for solving multi-dimensional Euler equations. To avoid numerical oscillations near shock waves, a slope limiter was adopted on complex boundary. Chaudhuri et al. [5] described the implementation of IBM and then applied it in conjunction with a fifth order classical WENO scheme to simulate the complex fluid-solid interactions. The simplified and modified ghost point treatments were introduced by Farooq et al. [6] for solving two dimensional compressible Euler equations based on Cartesian grids. Their methods were second order accurate near boundaries. Tan and Shu [7] developed a high order numerical boundary treatment, consisting of the inverse Lax-Wendroff type procedure for inflow boundary conditions and extrapolation for outflow boundary conditions, to solve hyperbolic conservation laws with finite difference methods. However, the algebra of the ILW procedure depended on partial difference equations (PDEs) was very heavy for practical applications. In [8], the boundary treatment proposed by Tan et al. [7] was further simplified and improved for efficient implementation in practice. This innovative boundary treatment procedure was demonstrated on the scheme with fifth order accuracy which was the same order as the internal WENO scheme. Vilar and Shu [9] generalized the ILW treatment for the inflow boundary of a linear hyperbolic problem and analyzed the stability of the resulting schemes.

The mechanism of detonation wave propagation in complex tubes was studied widely by many researchers, which is of great importance to industrial safety. Up to now, some experimental and numerical results are available. The experiment on gaseous detonation diffraction in a 90 degrees branched channel was investigated by the work of Guo et al. [10]. Starr et al. [11] performed studies on detonation limits in rough tubes. It was concluded that detonation limits in rough tubes were wider than that in smooth tubes.

Zhu et al. [12] experimentally investigated the effect of turning on explosion propagation in single bend, U-shaped and Z-shaped pipe, respectively. Zhang et al. [13] experimentally investigated the effect of branch tunnels on explosion propagation in five different tunnels. Frolov et al. [14] reported results of studies on initiation, propagation, and stability of gaseous detonation in U-shaped tubes by extensive experiments and numerical simulations. Hou et al. [15] built a mathematical model for explosion wave propagation in turn roadway. The numerical results showed that pressure, velocity and temperature are gradually attenuated during its propagation. Wang et al. [16] carried out a numerical simulation to investigate the effect of the obstacles on the explosion of the premixed gas by combining fifth order WENO scheme and two-step reaction model. Li et al. [17] numerically investigated the formation mechanism of cellular detonation propagating through pipe bends by a detailed reaction model. These simulations show that boundary treatment is very critical to investigation on both the detonation reflection near the rigid wall and detonation cellular size.

In this paper, the ILW boundary treatment with fifth order accuracy first was extended to the reactive Euler system with a two-step reaction model. Combining a fifth order LF-WENO scheme, a high order parallel code was developed to investigate the interactions of shock/detonation waves with the complex rigid boundaries of geometries and avoided effectively the nonphysical results in the simulations that are very sensitive to the boundary numerical treatment method. We further demonstrated and validated the efficient implementations of the ILW treatment by comparing the experimental results.

The remainder of this paper is organized as follows. Some non-dimensional parameters as well as governing equations are given in Section 2. Then we focus on the issue of extending fifth order ILW treatment to 2D two-step reactive Euler equations in Section 3. In Section 4 shock wave propagation through a rough tube with rectangular grooves is first simulated. Then we numerically investigate detonation wave propagation over a circular cylinder to compare the pressure histories and its peaks at several locations near the surface of cylinder utilizing the ILW treatment and IBM respectively for rigid walls. Finally, the effect of the obstacle width on cellular structure is discussed through investigating detonation wave propagation in a rough tube. Concluding remarks are given in Section 5.

2 Governing equations

The governing equations used for investigating detonation wave propagation are the two-step reactive Euler equations with source terms [18,19]. The chemical reaction is divided into two stages including the first induction period and the subsequent exothermic one. In a 2D Cartesian coordinate system, we consider strongly hyperbolic conservation laws including the two-step chemical reaction by neglecting the effects of viscosity, the heat diffusion, and body force. We choose three characteristic physical quantities includ-

ing the induction reaction length (l^*), the heat of reaction per unit mass (q) and the initial mass density (ρ_0). Thus, references for the velocity, the pressure, the temperature, the energy, and the time can be defined as

$$u^*=v^*=\sqrt{q},\quad p^*=\rho_0 q,\quad T^*=q/\widehat{R},\quad E^*=q\quad t^*=l^*/\sqrt{q}. \tag{2.1}$$

So the governing equations can be reduced to non-dimensional forms by using above references.

$$\frac{\partial U}{\partial t}+\frac{\partial F(U)}{\partial x}+\frac{\partial G(U)}{\partial y}=\phi(U), \tag{2.2}$$

$$U=\begin{bmatrix}\rho\\ \rho u\\ \rho v\\ \rho E\\ \rho\alpha\\ \rho\beta\end{bmatrix},\quad F=\begin{bmatrix}\rho u\\ \rho u^2+p\\ \rho uv\\ \rho u(E+p/\rho)\\ \rho u\alpha\\ \rho u\beta\end{bmatrix},\quad G=\begin{bmatrix}\rho v\\ \rho uv\\ \rho v^2+p\\ \rho v(E+p/\rho)\\ \rho v\alpha\\ \rho v\beta\end{bmatrix},\quad \phi=\begin{bmatrix}0\\ 0\\ 0\\ 0\\ \rho\omega_\alpha\\ \rho\omega_\beta\end{bmatrix}, \tag{2.3}$$

$$p=\rho T, \tag{2.4}$$

$$E=\frac{T}{\gamma-1}+\beta+\frac{1}{2}(u^2+v^2), \tag{2.5}$$

$$\omega_\alpha=\frac{d\alpha}{dt}=-k_1\rho\exp\Big(-\frac{E_1}{T}\Big), \tag{2.6}$$

$$\omega_\beta=\frac{d\beta}{dt}=\begin{cases}-k_2p^2\big(\beta^2\exp(-\frac{E_2}{T})-(1-\beta)^2\exp(-\frac{E_2+1}{T})\big), & \alpha\le 0,\\ 0, & \alpha>0,\end{cases} \tag{2.7}$$

where p, ρ, E, T, $\widehat{R}$, u and v denote non-dimensional pressure, density, total energy, temperature, gas constant and two Cartesian components of the velocity vector, respectively. The reaction progress parameters α and β are $0<\alpha<1$ and $\beta=1$ in the induction period, $\alpha\le 0$ and $0<\beta<1$ in the subsequent exothermic one. E_1 and E_2 denote activation energy. k_1 and k_2 present chemical reaction rate constants. The parameter γ defines the specific heat ratio. We set $E_1=1.71$, $E_2=0.347$, $k_1=27.7$, $k_2=7.69$ and $\gamma=1.4$ in the following simulations.

The semi-discrete approximation of (2.2) is given by

$$\left(\frac{\partial U}{\partial t}\right)_{i,j}=-\frac{1}{\Delta x}\big(\hat{F}_{i+1/2,j}-\hat{F}_{i-1/2,j}\big)-\frac{1}{\Delta y}\big(\hat{G}_{i,j+1/2}-\hat{G}_{i,j-1/2}\big)+\phi_{i,j}, \tag{2.8}$$

where $\hat{F}_{i+1/2,j}$ and $\hat{G}_{i,j+1/2}$ present the numerical fluxes, which are obtained by a fifth order finite difference WENO scheme with the Lax-Friedrichs splitting [20]. A third order TVD Runge-Kutta scheme is used to integrate the system of ordinary differential equations (2.8) in time.

3 Boundary treatment

The goal of this section is to extend the ILW procedure to the reactive Euler equations with a two-step reaction model. Assume that the values on the grid points in the interior of the computational domain have been updated from the previous time level with a fifth order WENO scheme. For a given ghost point P, a corresponding point P_0 on the complex boundary can be only determined such that the normal at P_0 goes through the ghost point P and points to the interior of the computational domain. Thus we can set up a local coordinate system at point P_0 so that the new $\hat{x}$-axis and the normal at P_0 have the same direction by

$$\begin{cases} \hat{x}=x\cos\theta+y\sin\theta, \\ \hat{y}=-x\sin\theta+y\cos\theta, \end{cases} \tag{3.1}$$

where θ denotes the angle between the old x-axis and the normal vector at P_0.

Utilizing Eq. (3.1), we can easily convert the reactive Euler equations (2.2) to the new forms in the local coordinate system as follows

$$\frac{\partial \hat{U}}{\partial t}+\frac{\partial F(\hat{U})}{\partial \hat{x}}+\frac{\partial G(\hat{U})}{\partial \hat{y}}=\phi(\hat{U}), \tag{3.2}$$

$$\hat{U}=\left[\hat{U}_1\ \hat{U}_2\ \hat{U}_3\ \hat{U}_4\ \hat{U}_5\ \hat{U}_6\right]^T=[\rho\ \rho\hat{u}\ \rho\hat{v}\ \rho E\ \rho\alpha\ \rho\beta]^T, \tag{3.3}$$

$$\begin{cases} \hat{u}=u\cos\theta+v\sin\theta, \\ \hat{v}=-u\sin\theta+v\cos\theta. \end{cases} \tag{3.4}$$

To achieve a fifth order accurate boundary treatment, the values of the ghost point P can be obtained by the Taylor expansion in the normal direction

$$(\hat{U}_m)_P\approx\hat{U}_m^{*(0)}+\hat{x}_P\hat{U}_m^{*(1)}+\frac{\hat{x}_P^2}{2}\hat{U}_m^{*(2)}+\frac{\hat{x}_P^3}{6}\hat{U}_m^{*(3)}+\frac{\hat{x}_P^4}{24}\hat{U}_m^{*(4)}, \qquad m=1,\cdots,6, \tag{3.5}$$

where $\hat{U}_m^{*(k)}$ represent the normal derivative of $\hat{U}_m$ at P_0 on the complex boundary.

Then we do a local characteristic decomposition for (3.2) to determine the inflow and outflow boundary conditions and choose a point P_1 closest to P_0 in the interior domain. So we define the Jacobian matrix at P_0 by

$$J=\left.\frac{\partial F(\hat{U})}{\partial \hat{U}}\right|_{P_1}. \tag{3.6}$$

Assuming that the six eigenvalues of (3.6) are $\lambda_1=\hat{u}-c$, $\lambda_2=\lambda_3=\lambda_4=\lambda_5=\hat{u}$ and $\lambda_6=\hat{u}+c$. The left characteristic matrix L consisting of a complete set of left eigenvectors of (3.6) is

given by

$$L(\hat{U}_{P_1}) = \left[l_{ij}\right]_{6\times 6}$$
$$= \frac{\gamma-1}{2\gamma T}\begin{bmatrix} \frac{u^2+v^2}{2}+\frac{u}{\tilde{c}}\frac{\gamma T}{\gamma-1} & -u-\frac{1}{\tilde{c}}\frac{\gamma T}{\gamma-1} & -v & 1 & 0 & -1 \\ -v\left(u^2+v^2\right) & 2uv & \frac{2\gamma T}{\gamma-1}+2v^2 & -2v & 0 & 2v \\ -\alpha\left(u^2+v^2\right) & 2\alpha u & 2\alpha v & -2\alpha & \frac{2\gamma T}{\gamma-1} & 2\alpha \\ -\beta\left(u^2+v^2\right) & 2\beta u & 2\beta v & -2\beta & 0 & \frac{2\gamma T}{\gamma-1}+2\beta \\ \frac{2\gamma T}{\gamma-1}-\left(u^2+v^2\right) & 2u & 2v & -2 & 0 & 2 \\ \frac{u^2+v^2}{2}-\frac{u}{\tilde{c}}\frac{\gamma T}{\gamma-1} & -u+\frac{1}{\tilde{c}}\frac{\gamma T}{\gamma-1} & -v & 1 & 0 & -1 \end{bmatrix}_{P_1}, \quad (3.7)$$

where the sound speed $\tilde{c}=\frac{1}{2}\sqrt{2u^2\gamma-2u^2\gamma^2+2v^2\gamma+4\gamma\beta-4\gamma^2\beta+4\gamma^2E-4\gamma E-2v^2\gamma^2}$.

So the local characteristic vector can be obtained by

$$\begin{bmatrix}\hat{V}_1\\ \hat{V}_2\\ \hat{V}_3\\ \hat{V}_4\\ \hat{V}_5\\ \hat{V}_6\end{bmatrix} = \begin{bmatrix} l_{11} & l_{12} & l_{13} & l_{14} & l_{15} & l_{16} \\ l_{21} & l_{22} & l_{23} & l_{24} & l_{25} & l_{26} \\ l_{31} & l_{32} & l_{33} & l_{34} & l_{35} & l_{36} \\ l_{41} & l_{42} & l_{43} & l_{44} & l_{45} & l_{46} \\ l_{51} & l_{52} & l_{53} & l_{54} & l_{55} & l_{56} \\ l_{61} & l_{62} & l_{63} & l_{64} & l_{65} & l_{66} \end{bmatrix}_{P_1} \begin{bmatrix}\hat{U}_1\\ \hat{U}_2\\ \hat{U}_3\\ \hat{U}_4\\ \hat{U}_5\\ \hat{U}_6\end{bmatrix}. \quad (3.8)$$

Because the main objective of this paper is to investigate the interactions between detonation waves and the complex rigid boundaries, the physical boundary condition $\hat{u}_{P_0}=0$ can be used in our simulations. So we can decide the signs of the six eigenvalues of (3.6), which decides the inflow and outflow boundary conditions.

If variable $\hat{V}$ is a local conservative characteristic vector, the normal derivatives $\hat{V}^{(k)}$ $(k=0,\cdots,4)$ at P_0 can be achieved by the fifth order WENO type extrapolation [8]. Substituting the prescribed boundary condition for the sixth equation of (3.8), we get a new linear system solved for $\hat{U}^{*(0)}$ as follows

$$\begin{pmatrix} l_{11} & l_{12} & l_{13} & l_{14} & l_{15} & l_{16} \\ l_{21} & l_{22} & l_{23} & l_{24} & l_{25} & l_{26} \\ l_{31} & l_{32} & l_{33} & l_{34} & l_{35} & l_{36} \\ l_{41} & l_{42} & l_{43} & l_{44} & l_{45} & l_{46} \\ l_{51} & l_{52} & l_{53} & l_{54} & l_{55} & l_{56} \\ 0 & 1 & 0 & 0 & 0 & 0 \end{pmatrix} \begin{bmatrix}\hat{U}_1^{*(0)}\\ \hat{U}_2^{*(0)}\\ \hat{U}_3^{*(0)}\\ \hat{U}_4^{*(0)}\\ \hat{U}_5^{*(0)}\\ \hat{U}_6^{*(0)}\end{bmatrix} = \begin{bmatrix}\hat{V}_1^{(0)}\\ \hat{V}_2^{(0)}\\ \hat{V}_3^{(0)}\\ \hat{V}_4^{(0)}\\ \hat{V}_5^{(0)}\end{bmatrix}. \quad (3.9)$$

The sixth equation was replaced because the sixth equation corresponds to the inflow component. Our local coordinate system is defined in such a way that the new x-axis points to the interior of the computational domain. Therefore, the positive eigenvalue corresponds to the inflow component.

Combining the two-step reactive Euler equations (3.2) with the ILW procedure [7,8], we can get

$$\frac{(\gamma-1)}{2}\frac{\hat{U}_3^{*2}}{\hat{U}_1^{*2}}\hat{U}_1^{*(1)}+(1-\gamma)\frac{\hat{U}_3^{*}}{\hat{U}_1^{*}}\hat{U}_3^{*(1)}+(\gamma-1)\hat{U}_4^{*(1)}+(1-\gamma)\hat{U}_6^{*(1)}=\hat{U}_3^{*2}/\left(R\hat{U}_1^{*}\right), \quad (3.10)$$

where R is the radius of curvature at P_0 on the complex boundary.

From the local flow characteristics, we replace the sixth equation of (3.8) with (3.10). Thus, the values of $\hat{U}^{*(1)}$ can be solved by the following linear system

$$\begin{pmatrix} l_{11} & l_{12} & l_{13} & l_{14} & l_{15} & l_{16} \\ l_{21} & l_{22} & l_{23} & l_{24} & l_{25} & l_{26} \\ l_{31} & l_{32} & l_{33} & l_{34} & l_{35} & l_{36} \\ l_{41} & l_{42} & l_{43} & l_{44} & l_{45} & l_{46} \\ l_{51} & l_{52} & l_{53} & l_{54} & l_{55} & l_{56} \\ \frac{(\gamma-1)}{2}\frac{\hat{U}_3^{*2}}{\hat{U}_1^{*2}} & 0 & (1-\gamma)\frac{\hat{U}_3^{*}}{\hat{U}_1^{*}} & \gamma-1 & 0 & 1-\gamma \end{pmatrix}\begin{bmatrix} \hat{U}_1^{*(1)} \\ \hat{U}_2^{*(1)} \\ \hat{U}_3^{*(1)} \\ \hat{U}_4^{*(1)} \\ \hat{U}_5^{*(1)} \\ \hat{U}_6^{*(1)} \end{bmatrix}=\begin{bmatrix} \hat{V}_1^{(1)} \\ \hat{V}_2^{(1)} \\ \hat{V}_3^{(1)} \\ \hat{V}_4^{(1)} \\ \hat{V}_5^{(1)} \\ \hat{U}_3^{*2}/R\hat{U}_1^{*} \end{bmatrix}. \quad (3.11)$$

The values of $\hat{U}^{*(k)}$ $(k=2,3,4)$ can be easily achieved by the following extrapolation equations where the ILW procedure is not needed

$$\begin{pmatrix} l_{11} & l_{12} & l_{13} & l_{14} & l_{15} & l_{16} \\ l_{21} & l_{22} & l_{23} & l_{24} & l_{25} & l_{26} \\ l_{31} & l_{32} & l_{33} & l_{34} & l_{35} & l_{36} \\ l_{41} & l_{42} & l_{43} & l_{44} & l_{45} & l_{46} \\ l_{51} & l_{52} & l_{53} & l_{54} & l_{55} & l_{56} \\ l_{61} & l_{62} & l_{63} & l_{64} & l_{65} & l_{66} \end{pmatrix}\begin{bmatrix} \hat{U}_1^{*(k)} \\ \hat{U}_2^{*(k)} \\ \hat{U}_3^{*(k)} \\ \hat{U}_4^{*(k)} \\ \hat{U}_5^{*(k)} \\ \hat{U}_6^{*(k)} \end{bmatrix}=\begin{bmatrix} \hat{V}_1^{(k)} \\ \hat{V}_2^{(k)} \\ \hat{V}_3^{(k)} \\ \hat{V}_4^{(k)} \\ \hat{V}_5^{(k)} \\ \hat{V}_6^{(k)} \end{bmatrix}. \quad (3.12)$$

Using the above five linear systems comprising (3.9), (3.11) and (3.12), we can obtain the values of normal derivatives $\hat{U}^{*(k)}$ $(k=0,1,2,3,4)$. Therefore, the values of the ghost points can be imposed by the Taylor expansion (3.5) and the rotated coordinate system (3.4).

4 Numerical simulation

4.1 The validation of the ILW treatment

In our previous paper [8], we have demonstrated that the ILW treatment is a fifth order accurate boundary treatment, which is the same as order as our interior WENO scheme. The main goal of this subsection is to demonstrate the validation of the ILW treatment by comparing our numerical results with the experimental ones. Gongora-Orozco et al. [21] experimentally investigated the shock wave propagation, which usually involves the

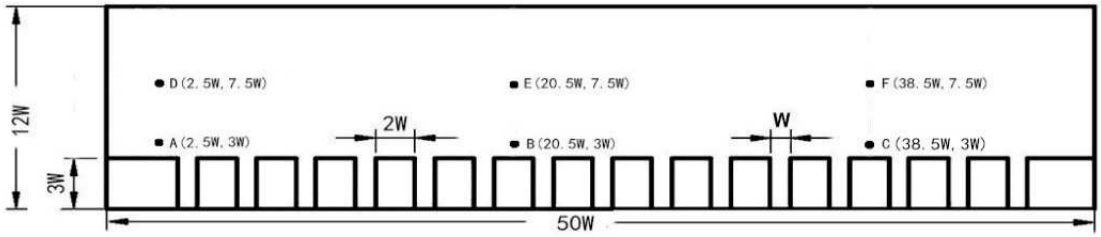

Figure 1: Computational configuration of shock wave propagation through a rough tube.

complex physical mechanisms such as the shock reflections, diffractions, shock-vortex interactions and so on. The computational model is shown in Fig. 1, which is the same as their experimental model. Note that in this particular example, we can easily apply the standard reflection technique to treat the boundaries of the rectangular grooves. However, for more complex geometries presented later and straight wall boundary not located at the center of adjacent grid points, the application of the reflection technique is not straightforward, while we can successfully apply the ILW treatment.

In the simulation, the computational domain divided by a uniform Cartesian mesh with mesh size $\Delta x = \Delta y = 0.02$ is 50×12. We set up 15 rectangular grooves on the lower wall, while the upper wall of the tube is smooth. The width and height of rectangular grooves are 1 and 3, respectively. The width of rectangular obstacles is 2. The left boundary is inflow condition, the right boundary is outflow condition, and other boundaries are rigid wall treated by the fifth order ILW treatment. The initial incident shock wave with a Mach number of $M_s = 1.66$ is located on the left, and travels downstream to the right exit of the rough tube.

From Fig. 2, we can see that, when the incident shock wave propagating inside a rough tube encounters each groove, diffraction and reflection will occur. When arriving at the exit of the tube, the intricate shock wave patterns behind the incident shock wave can be seen due to the interactions of shock waves with grooves and other smooth rigid walls. Fig. 2(a) represents the experimental result captured by the high-speed schlieren photography technique. Fig. 2(b) shows our numerical result. For comparison between our numerical result and the experimental one, we divide it into three parts, i.e., zone ZA, zone ZB and zone ZC, as shown in Fig. 2. Before the incident shock wave exit the test section, the reflected waves from the smooth upper wall are diffracted continuously by grooves in zone ZA. Thus the pressure gradient in zone ZA decreases gradually, which makes the shock wave patterns in zone ZA more ambiguous. We can see from Fig. 2 that zone ZB has very clear shock wave patterns because the reflected contributions from both the upper wall and rectangular obstacles on the lower wall are stronger than the diffraction of mounted-wall grooves. The shock wave patterns of zone ZC are more intricate than other parts due to the interactions of the reflected waves from the upper wall and the rectangular obstacles. Comparing Fig. 2(a) with Fig. 2(b), excellent agreement in the corresponding zones is observed between the numerical and experimental

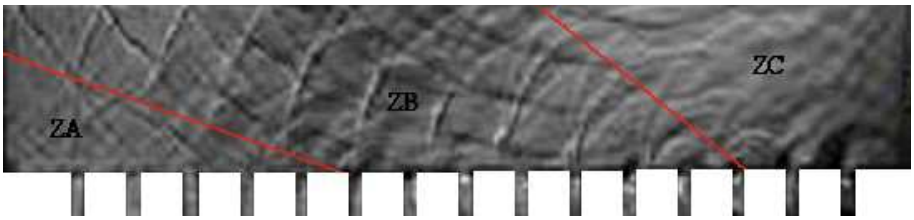

(a) Schlieren image obtained by experiment [21]

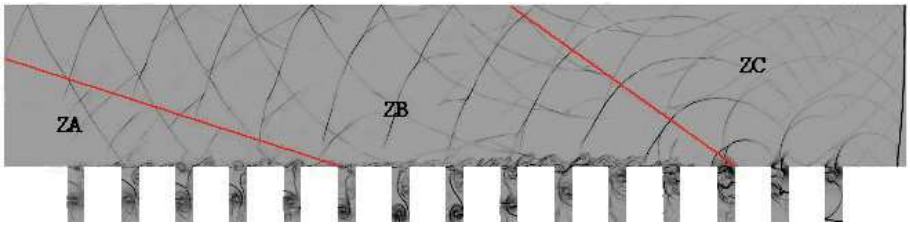

(b) Schlieren image obtained by the ILW treatment

Figure 2: Experimental and our numerical results of shock wave propagation through a rough tube.

results, which further demonstrates that the ILW treatment can reflect the intrinsic physical mechanism of the interactions among the incident shock wave, wall-mounted grooves and the smooth walls.

4.2 The comparison between the ILW treatment and the IBM

To investigate the influences of different orders of boundary treatment techniques on the internal flow field, we apply the fifth order WENO scheme in the internal computational domain, and adopt our fifth order ILW treatment and the second order IBM [5] to treat all rigid walls, respectively. Five transducers near the surface of circular cylinder are located as shown in Fig. 3 to monitor the pressure history of propagating detonation waves.

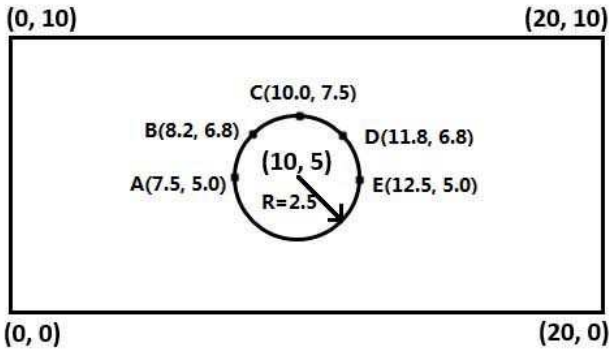

Figure 3: Computational configuration of detonation wave propagation over a circular cylinder in a tube.

A computational domain divided by a uniform Cartesian mesh with mesh size $\Delta x = \Delta y = 0.017$ is 20×10 as shown in Fig. 3. A circular cylinder with the radius of $R = 2.5$ is located at $(10,5)$. The tube is filled with a stoichiometric hydrogen-oxygen mixture. The non-dimensional initial state is $(\rho,u,v,p,\alpha,\beta) = (1,0,0,0.16,1,1)$. The left boundary is inflow condition, and the right boundary is outflow condition. The upper and low boundaries and the surface of cylinder are assumed to be rigid walls treated by the ILW treatment and IBM, respectively. A Zeldovich, Von Neumann and Doering (ZND) profile is initially located at the entrance as the inflow boundary condition. See [22, 23] for more details about the ZND profile. The outlet adopts the free outflow boundary condition.

Fig. 4 represents the pressure histories of the different monitoring locations near the surface of the circular cylinder. From Fig. 4(a), it can be seen that the first pressure peak occurs at time 4.1, which indicates that normal reflection happens at point A. Then detonation wave collides with the surface of the cylinder at point B and is reflected at time 4.8. The corresponding pressure peak of point B occurs as shown in Fig. 4(b). The reflected wave travels in the opposite direction and then arrives and reflects again at the upper rigid wall, which makes pressure increase slightly after time 12.4 elapse at point B. When detonation front passes over point C, diffraction occurs as shown in Fig. 4(c). Fig. 4(d) shows that the magnitude of pressure at point D increases to 0.75, and then the second pressure peak appears due to the reflected wave from the upper rigid wall. However, pressure will be reduced dramatically by rarefaction effect at point D. Diffracted waves propagate from the top and the bottom to the center of the tube at the same time, and then collide with each other, which makes a transient pressure increase. Due to the contribution of rarefaction waves at point E, the shock pressure drops down in a short time as shown in Fig. 4(e). Next we compare the differences of pressure histories at five points to analyze the influences on the internal flow field under the different boundary treatment techniques. At point A, the pressure peak (5.74) obtained by the ILW treatment is obviously lower than IBM (7.88), as shown in Fig. 4(a). On the contrary, the pressure peak (4.37) obtained by our numerical boundary treatment is apparently higher than IBM (3.53) at point B, as shown in Fig. 4(b). However, the rest of points almost have the same pressure histories, i.e., pressure peaks obtained by the ILW treatment are almost the same as that by IBM at these points. From what has been discussed above, it can be concluded that different orders of boundary treatment techniques doubtlessly have a major impact on the internal flow characteristics such as pressure; the influence on pressure peaks in the reflected zone is obviously bigger than that in the diffracted zone. Thus we use the fifth order ILW procedure rather than lower order boundary treatments to treat all rigid walls to avoid polluting the numerical results in the following simulations.

4.3 Implementation of the ILW treatment in detonation

In this section, we are of great interest to implement the high order ILW procedure to investigate the interactions between detonation waves and complex obstacles.

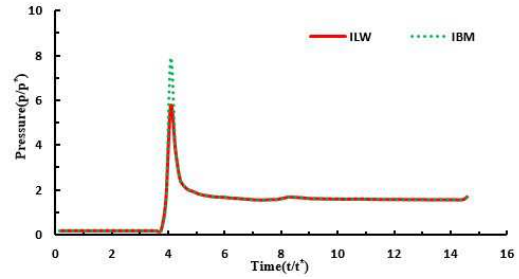

(a) The pressure history of monitoring point A

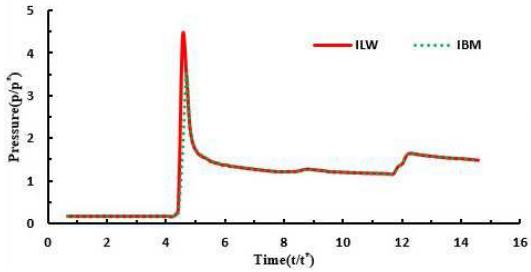

(b) The pressure history of monitoring point B

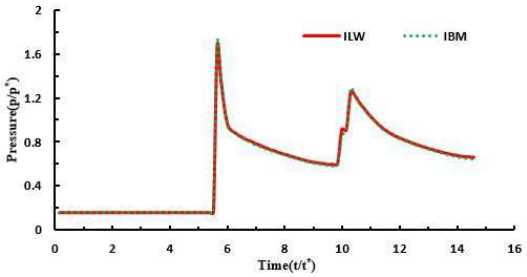

(c) The pressure history of monitoring point C

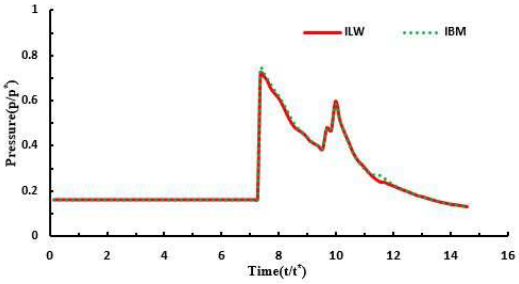

(d) The pressure history of monitoring point D

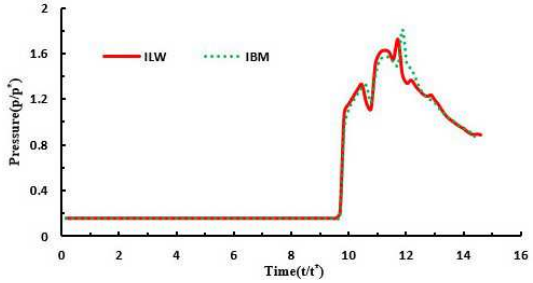

(e) The pressure history of monitoring point E

Figure 4: The pressure histories of monitoring point A-E: red solid line represents the pressure histories obtained by the ILW treatment; green dotted line represents the pressure histories obtained by the IBM.

4.3.1 Detonation wave propagation over a triangular prism

This example investigates detonation wave propagation over a triangular prism inside a tube. The computational domain divided by a uniform Cartesian mesh with mesh size $\Delta x = \Delta y = 0.017$ is 20×8 as shown in Fig. 5. Three apices of the triangular prism embedded in a tube are $(0,0)$, $(3.4,1.9)$ and $(3.4,-1.9)$, respectively. The initial and boundary conditions are the same as Subsection 4.2. The high order ILW treatment are also used for all rigid walls including the surface of the triangular prism.

Fig. 6(a) shows that detonation wave first collides and reflects at the apex of a triangular prism at time 0.92. The local high temperature and high pressure zone occurs,

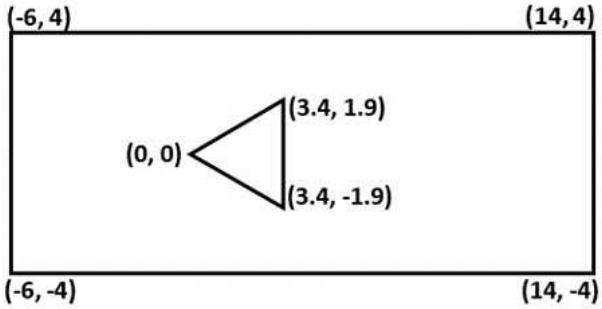

Figure 5: Computational configuration of detonation wave propagation over a triangular prism in a tube.

leading to much chemical energy, which endlessly promotes detonation wave propagation. It can be seen from Fig. 6(b) that Mach stems form due to the reflection of detonation front on the upper and lower surfaces of the prism. Diffraction occurs when detonation front arrives at the upper and low apices of the prism as shown in Fig. 6(c). At time 1.62, low pressure zones located at the posterior of the prism are obviously observed. The reflected waves collide with the upper and lower rigid wall and are reflected again. At time 2.28, the collision of diffracted waves cause a local high temperature and high pressure zone igniting the combustible gas. Subsequently, the pressure at the back of the prism decreases dramatically due to the contribution of rarefaction waves, and the low pressure zone enlarges over time. It can be seen from Fig. 6(f) that two small vortexes move forward along the horizontal direction at upper and lower apices of prism, and a large low pressure zone also appears at the back of the prism.

4.3.2 Influences of rectangular obstacles with different widths on detonation wave propagation

The computational models similar to Subsection 4.1 are adopted to investigate the influences of different width of rectangular obstacles on propagating detonation wave in the following simulations. The whole non-dimensional computational domain is 132×32 and divided by a uniform Cartesian mesh with $\Delta x=\Delta y=0.02$. The widths of the obstacles for three cases are 5 (case 1), 2.5 (case 2) and 0.75 (case 3), respectively. We set up 15, 22 and 43 rectangular grooves on the lower wall for the respective case 1, case 2 and case3, with the same left wall locations of the first grooves on the left for three cases. The initial conditions for investigating detonation wave propagation are identical to those in Subsection 4.2. The left and right boundaries are described as the inflow and outflow conditions, respectively. Other boundaries are assumed to be rigid walls treated by the fifth order ILW treatment.

In Fig. 7(a), it can be seen that detonation front encounters the first groove on the lower wall. When detonation wave reaches the left side of the first rectangular obstacle, the reflected waves will appear as shown in Fig. 7(b). Obviously the first vortex appears at the left side of the first groove, and the lower part of detonation front curves back-

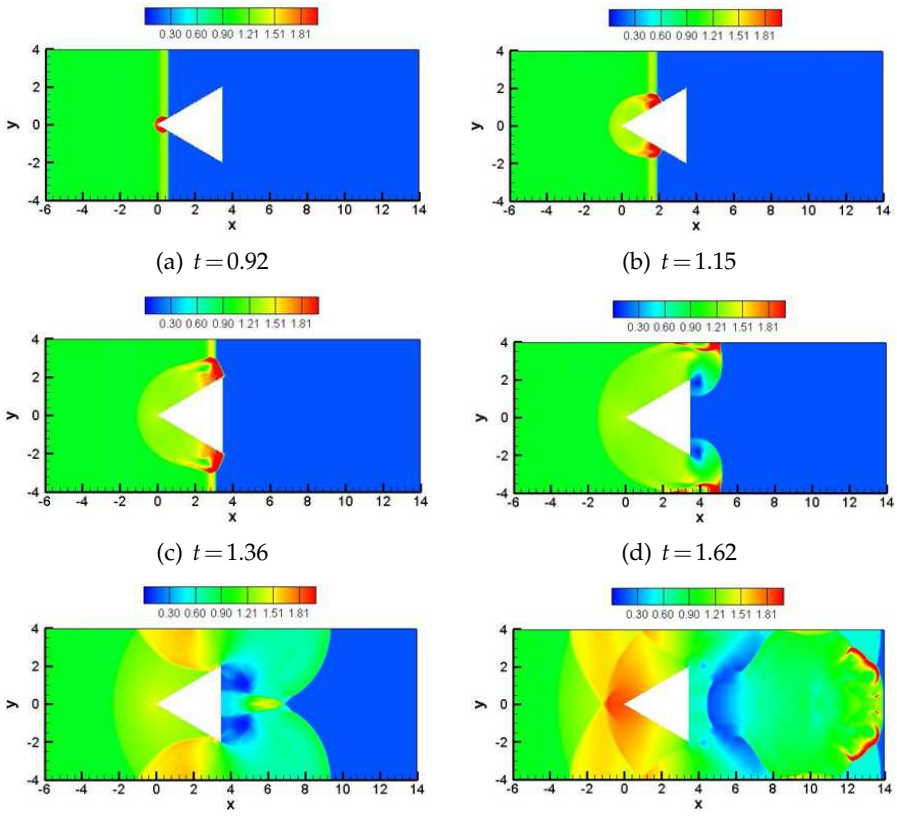

(a) $t=0.92$ (b) $t=1.15$

(c) $t=1.36$ (d) $t=1.62$

(e) $t=2.28$ (f) $t=3.34$

Figure 6: Pressure contours of detonation wave propagation over a triangular prism in a tube.

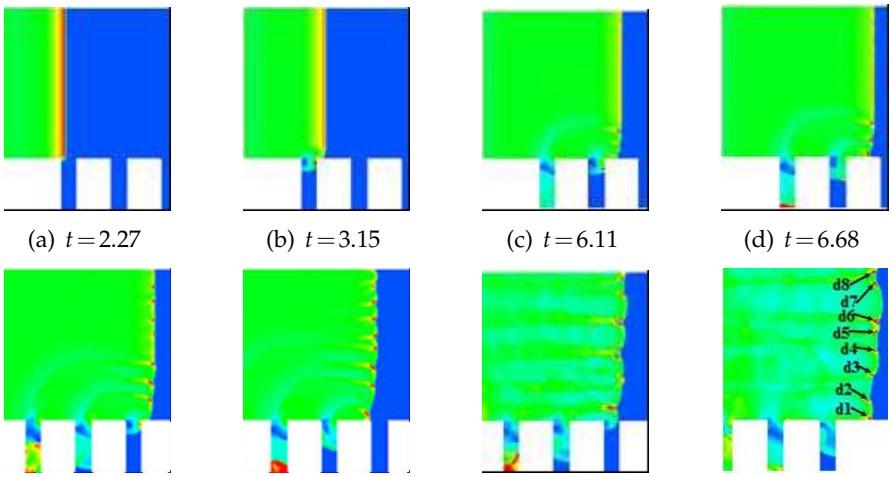

(a) $t=2.27$ (b) $t=3.15$ (c) $t=6.11$ (d) $t=6.68$

(e) $t=8.52$ (f) $t=9.89$ (g) $t=30.09$ (h) $t=43.44$

Figure 7: Pressure contours of detonation wave propagation in a tube with grooves.

ward. As the part of detonation wave travels toward grooves, detonation decays and the front decouples with reaction zone. There are some obvious triple points on detonation front when propagating though the tube, which releases a lot of chemical energy making the curved front on the lower part propagate quickly, as shown in Fig. 7(c). Over time, diffracted wave arrives at the bottom of the first cavity and is reflected, which causes a local high temperature and high pressure zone. The unburned gas is re-ignited and then exhausted in the first groove. The transverse perturbations caused by a series of obstacles make inhomogeneous flow and energy release inside the detonation front. The cellular detonations are observed as shown in Fig. 7(e). In Fig. 7(f), a group of triple points forms at detonation front. Since triple points are destroyed constantly by the obstacles, the number of triple points decreases as shown in Fig. 7(g), while the triple points become strong as shown in Fig. 7(h).

Fig. 8 display the pressure of the detonation front at time 43.44. Eight peaks (d1-d8) appear on the pressure curve, which are the same as the numbers and locations of Fig. 7(h). Pressure histories at A, B, C, D, E and F for the three different cases are presented in Fig. 9. It should be noted that the six locations (A-F) mentioned above for the three cases are $(6.25,10)$, $(51.25,10)$, $(96.25,10)$, $(6.25,18.75)$, $(51.25,18.75)$ and $(96.25,18.75)$, respectively. At time 3.57, the pressure peak of point A is 1.68, which is the same as point D, because these monitoring points locate before the first cavity. At time 17.05, the pressure at point A decreases slightly due to the contribution of grooves. The pressure peaks appear simultaneously at point B and E, and are 1.09 and 1.26 respectively, as shown in Fig. 9(a). The pressure peak (1.03) at point F appears before point C (1.14). Numerical results of Case 1 indicate that the pressure at detonation front decreases gradually. In Fig. 9(b), the pressure peak at point E appears ahead of point B, and they are 1.34 and 1.36, respectively. As time goes on, the pressure peaks of point C and point F occur at the same time and equal to 1.16 and 1.35, respectively. Comparing the pressure peaks at six points for case 2, we can conclude that the pressure of detonation front near obstacles decreases over time; the pressure of detonation front far away from the lower wall first decreases and then increases. It can be seen from Fig. 9(c) that the monitoring points E

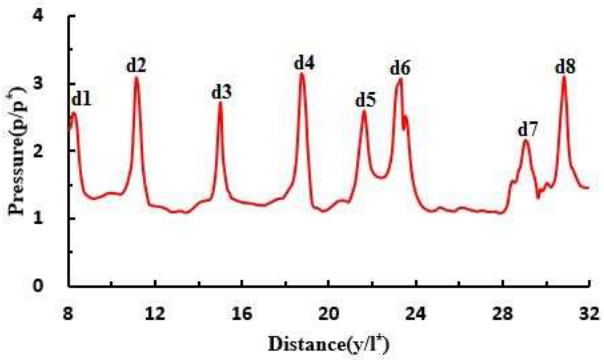

Figure 8: Pressure of detonation front at $t=43.44$.

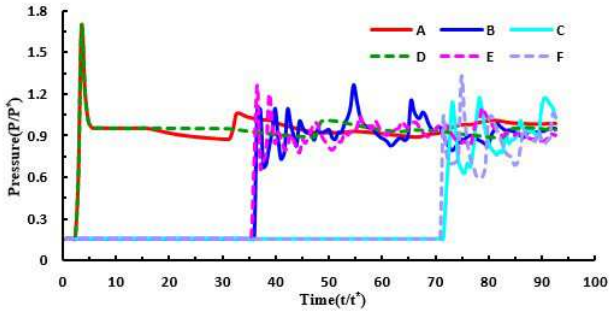

(a) Pressure histories for case 1

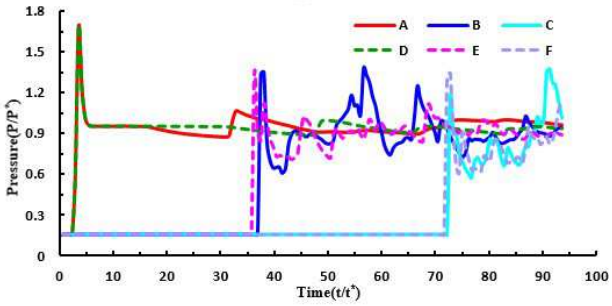

(b) Pressure histories for case 2

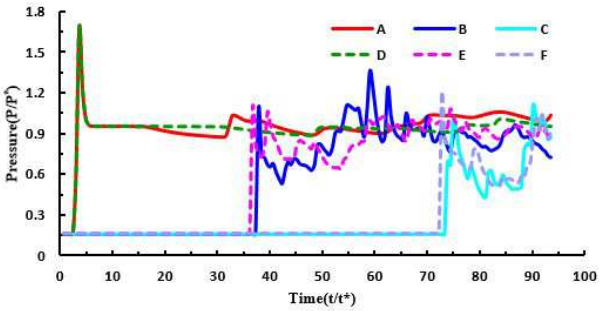

(c) Pressure histories for case 3

Figure 9: Pressure histories for case 1-3.

and B have the same pressure peak 1.08; the pressure peak (1.19) at point F is a little bigger than that at point C (1.01). The evolution of detonation front for case 3 is similar to case 2. As discussed above, we can find that, with the reduction of the upper width of rectangular obstacles, the pressure of detonation front increases first and then decreases in the interior physical domain. Fig. 10 represents the maximum pressure history by simulating numerically the smoke foil tracks. Comparing Fig. 10(a)-(c), it is clear that cellular structures become big and irregular with the decrease of the upper width of the rectangular obstacles.

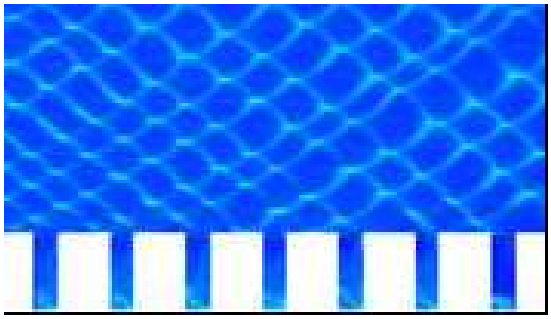

(a) Cellular structure for case 1

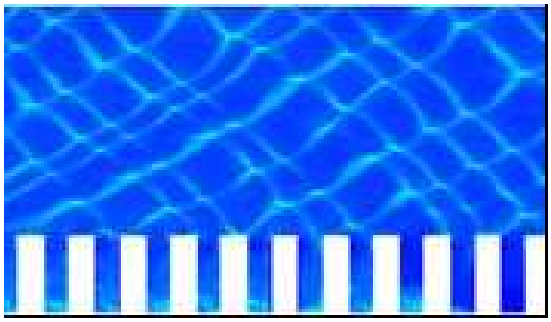

(b) Cellular structure for case 2

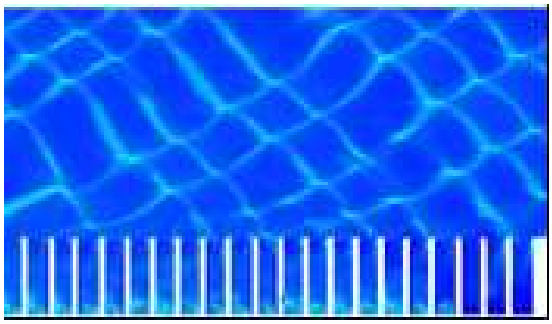

(c) Cellular structure for case 3

Figure 10: Cellular structures for case 1-3.

5 Conclusion

In our simulations, a fifth order ILW boundary procedure is extended to the reactive Euler equations to construct a high order boundary treatment for complex boundaries. The conclusions based on our numerical results are as follows:

1. The numerical results using the extended high order ILW procedure agree well with the experimental ones, which can reflect the intricate interaction laws of detonation waves with complex obstacles.

2. Numerical comparison shows that the pressure peaks achieved by the two kinds of boundary treatments mentioned above have obvious differences in the reflected zone, while there are no significant distinctions between these boundary treatments in the rarefaction zone.

3. The further off the rectangular obstacles, the smaller influences will occur for the internal reactive flow. The pressure of detonation front near rectangular obstacles decreases gradually as time goes by, while the pressure of detonation front far away from the lower wall first decreases and then increases. We also find that, with the reduction of the upper width of obstacles, the magnitude of detonation pressure increases first and then decreases at the same location in the internal reactive flow, that is to say, there exists an appropriate width of obstacles making the pressure peak reach its maximum. The numerical results also indicate that cellular size becomes small and regular with the increase of the width of the rectangular obstacles.

Acknowledgments

This research is supported by the National Natural Science Foundation of China under grants 11325209, 11221202 and 11402137, and the Foundation of State Key Laboratory of Explosion Science and Technology (Grant No. ZDKT11-01).

References

[1] I. O. Bohachevsky, A direct method for computation of nonequilibrium flows with detached shock waves, AIAA, 4 (1966), 600-607.
[2] G. Moretti, Importance of boundary conditions in the numerical treatment of hyperbolic equations, Phys. Fluids, II (1969), 13-20.
[3] C. S. Peskin. Flow patterns around heart values, A numerical method, J. Comput. Phys., 10 (1972), 252-271.
[4] B. Sjögreen, N. Petersson, A Cartesian embedded boundary method for hyperbolic conservation laws, Commun. Comput. Phys., 2 (2007), 1199-1219.
[5] A. Chaudhuri, A, Hadjadj, A. Chinnayya, On the use of immersed boundary methods for shock/obstacle interactions, J. Comput. Phys., 230 (2011), 1731-1748.
[6] M. A. Farooq, A. A. Skien, B. Müller, Cartesian grid method for the compressible Euler equations using simplified ghost points treatments at embedded boundaries, Comput Fluids, 82 (2013), 50-62.
[7] S. Tan, C.-W. Shu, Inverse Lax-Wendroff procedure for numerical boundary conditions of conservation laws, J. Comput. Phys., 229 (2010), 8144-8166.
[8] S. Tan, C. Wang, C.-W. Shu, J. Ning, Efficient implementation of high order inverse Lax-Wendroff boundary treatment for conservation laws, J. Comput. Phys., 231 (2012), 2510-2517.
[9] F. Vilar, C.-W. Shu, Development and stability analysis of the inverse Lax-Wendroff boundary treatment for central compact schemes, Math. Model Num., 49 (2015), 39-67.

[10] C. M. Guo, C. J. Wang, S. L. Xu, H. H. Zhang, Cellular pattern evolution in gaseous detonation diffraction in a 90°-branched channel, Combust. Flame, 148 (2007), 89-99.
[11] A. Starr, J. H. S. Lee, H. D. Ng, Detonation limits in rough walled tubes, Proc. Combust. Inst., 35 (2015), 1989-1996.
[12] C. J. Zhu, B. Q. Lin, Q. Ye, C. Zhai, Effect of roadway turnings on gas explosion propagation characteristics in coal mines, J. China U. Min. Techno., 21 (2012), 365-369.
[13] P. L. Zhang, Y. Du, Yi. Zhou et al., Explosions of gasoline-air mixture in the tunnels containing branch configuration, J. Loss. Prevent Proc., 26 (2013), 1279-1284.
[14] S. M. Frolov, V. S. Aksenov, I. O. Shamshin, Reactive shock and detonation propagation in U-bend tubes, J. Loss. Prevent Proc., 20 (2007), 501-508.
[15] W. Hou, Z. M. Qu, L. J. Pian, Numerical simulation on propagation and attenuation of shock waves in simplex turn roadway during gas explosion, J. China Coal Soc., 3 (2009), 509-513.
[16] C. Wang, T. B. Ma, J. Lu, Influence of obstacle disturbance in a duct on explosion characteristics of coal gas, Sci. China Phys. Mech., 2 (2010), 269-278.
[17] J. Li, H. L. Ren, J. G. Ning, Numerical application of additive Runge-Kutta methods on detonation interaction with pipe bends, Int. J. Hydrogen Energ., 38(2013), 9016-9027.
[18] S. Taki, T. Fujiwara, Numeical analysis of two-dimensional nonsteady detonation, AIAA, 16 (1978), 73-77.
[19] C. Wang, W. H. Han, J. G. Ning, Design and development of dynamic parallel computing code for three-dimensional gaseous detonation, Chinese J. Comput. Mech., 29 (2012), 948-953.
[20] G. S. Jiang, C.-W. Shu, Efficient implementation of weighted ENO schemes, J. Comput. Phys., 126 (1996), 202-228.
[21] N. Gongora-Orozco, H. Zare-Behtash, K. Kontis, Experimental Studies on Shock Wave Propagating Through Junction with Grooves, Proceedings of the 47th AIAA Aerospace Sciences Meeting Including New Horizons Forum and Aerospace Exposition, Florida, USA: American Institute of Aeronautics and Astronautics, 2009, 5-8.
[22] A. Bourlioux, A. J. Majda, Theoretical and numerical structure of unstable detonations, Philosophical Transactions of the Royal Society of London A, 350 (1995), 2968.
[23] Z. C. Zhang, S. T. J. Yu, H. He, S. C. Chang, Direct calculations of two- and three-dimensional detonations by an extended CE/SE method, AIAA, No.2001-0476.